Journal of Materials Chemistry

Cite this: *J. Mater. Chem.*, 2011, **21**, 11392

www.rsc.org/materials

PAPER

Synthesis–structure–performance correlation for polyaniline–Me–C non-precious metal cathode catalysts for oxygen reduction in fuel cells

Gang Wu,[a] Christina M. Johnston,*[a] Nathan H. Mack,[b] Kateryna Artyushkova,[c] Magali Ferrandon,[d] Mark Nelson,[a] Juan S. Lezama-Pacheco,[e] Steven D. Conradson,[e] Karren L. More,[f] Deborah J. Myers[d] and Piotr Zelenay*[a]

Received 23rd October 2010, Accepted 20th December 2010
DOI: 10.1039/c0jm03613g

In this report, we present the systematic preparation of active and durable non-precious metal catalysts (NPMCs) for the oxygen reduction reaction in polymer electrolyte fuel cells (PEFCs) based on the heat treatment of polyaniline/metal/carbon precursors. Variation of the synthesis steps, heat-treatment temperature, metal loading, and the metal type in the synthesis leads to markedly different catalyst activity, speciation, and morphology. Microscopy studies demonstrate notable differences in the carbon structure as a function of these variables. Balancing the need to increase the catalyst's degree of graphitization through heat treatment *versus* the excessive loss of surface area that occurs at higher temperatures is a key to preparing an active catalyst. XPS and XAFS spectra are consistent with the presence of Me–N_x structures in both the Co and Fe versions of the catalyst, which are often proposed to be active sites. The average speciation and coordination environment of nitrogen and metal, however, depends greatly on the choice of Co or Fe. Taken together, the data indicate that better control of the metal-catalyzed transformations of the polymer into new graphitized carbon forms in the heat-treatment step will allow for even further improvement of this class of catalysts.

Introduction

Polymer electrolyte fuel cells (PEFCs) operated on hydrogen fuel and air (*i.e.*, oxygen) are considered a viable technology for powering vehicles, among other applications. The cost of the platinum catalysts is prohibitive in PEFCs, especially at the high loadings required for the oxygen reduction reaction (ORR).[1] As a result, the development of non-precious metal catalysts (NPMCs) with high ORR activity has become a major focus of the PEFC research.[1] Early work examined the pyrolysis of transition metal-containing macrocycles,[2,3] resulting in ORR catalysts with promising yet insufficient activity and durability. Later studies replaced the expensive macrocycle precursors with a wide variety of common nitrogen-containing chemicals (ammonia, acetonitrile, amines, *etc.*), transition metal inorganic salts (sulfates, nitrates, acetates, hydroxides and chlorides), and carbon supports (Vulcan XC-72, Ketjenblack, Black Pearls, *etc.*).[4–10] From these studies, it was learned that the heat treatment of almost any mixture of (1) nitrogen, (2) carbon, and (3) metal precursors will result in a material that is ORR active; however, the degree of activity and durability depend greatly on the selection of precursors and synthesis chemistry.[3,11]

Although great advances have been recently made, no single material yet meets both the activity and durability requirements of fuel cell operation.[8,12,13] Several NPMCs with high activity have been reported since 2008, reaching volumetric performance in fuel cell tests of up to 50 and 98 A cm^{-3} at 0.80 V, respectively (values extrapolated from Tafel plots),[8,14] but with insufficient durability. Recently, we reported on a family of non-precious metal catalysts that utilized polyaniline (PANI) as a precursor to a carbon–nitrogen template for high-temperature synthesis of catalysts incorporating iron and cobalt.[15] The most active materials in the group catalyze the ORR at potentials within *ca.* 60 mV of that delivered by state-of-the-art carbon-supported platinum, combining their high activity with remarkable performance stability for non-precious metal catalysts (around 700 hours at a fuel cell voltage of 0.4 V), and excellent four-electron selectivity (H_2O_2 yield < 1.0%). Although the pace of recent progress is quite encouraging, further improvement is required before NPMCs can replace platinum catalysts.

[a]*Materials Physics and Applications Division, Los Alamos National Laboratory, Los Alamos, NM, 87545, USA. E-mail: cjohnston@lanl.gov; Tel: +1 505-667-4900. E-mail: zelenay@lanl.gov; Tel: +1 505-667-0197*
[b]*Chemistry Division, Los Alamos National Laboratory, Los Alamos, NM, 87545, USA*
[c]*Department of Chemical and Nuclear Engineering, University of New Mexico, Albuquerque, NM, 87131, USA*
[d]*Chemical Sciences and Engineering Division, Argonne National Laboratory, Argonne, Illinois, 60439, USA*
[e]*Materials Science and Technology Division, Los Alamos National Laboratory, Los Alamos, NM, 87545, USA*
[f]*Materials Science and Technology Division, Oak Ridge National Laboratory, Oak Ridge, TN, 37831, USA*

A designed approach to creating active and durable NPMCs based on the nature of the active site(s) would be desirable, but no conclusive description of active site(s) has yet been presented for the above described[15] or any other NPMCs prepared by heat treatment.[5–9,13,16–18] Experimental characterization and identification of active sites remain a challenge, because NPMCs prepared by heat treatment are inherently highly heterogeneous. Additionally complicating the analyses is the fact that species at the surface—defined in this context as the topmost atomic layer—are much more important for catalysis than the bulk composition, and no suitable surface probes for NPMCs have yet been developed. A vigorous debate has thus ensued regarding whether metal atoms participate directly in active sites,[5,8,10,19,20] or merely catalyze the formation of active sites from carbon, nitrogen, and perhaps oxygen atoms.[17,21–23] Metals could also play a secondary role by forming metal oxides that decompose peroxide.[18,24] Importantly, nearly all proposed active site structures involve nitrogen incorporated into carbon, whether the nitrogen species are bound to metal centers or not. Although catalysts with a certain degree of activity for the ORR can be prepared without any detectable metal content,[23,25] the presence of metal is essential to generate the most active and durable catalysts known to date.[8,15] Since the amount of atomically dispersed metal required to populate active sites is theoretically very small, it is difficult to reach a convincing conclusion with respect to the participation of metal atoms in active centers.[8,15] It also remains unclear that different families of active NPMCs should necessarily have the same types of active sites, although a correlation between catalyst microporosity and activity across nine samples from seven different laboratories has been found in a 2009 publication.[10]

Within this complicated context, we report here a systematic study on the PANI-derived ORR catalyst that correlates the morphology and chemical speciation obtained from different synthetic paths with the resulting catalyst activity, in order to guide further development of such non-precious metal catalysts. Variation of the synthesis steps, heat-treatment temperature, metal loading, and the transition metal results in catalysts with markedly different activity, composition, and structure. Extensive characterization results are introduced in this report to provide insight into the origin of enhanced catalytic performance observed with the PANI-derived catalyst. More comprehensive X-ray absorption results will be presented in a forthcoming publication.[26]

Experimental

Catalyst synthesis

Ketjenblack EC 300J (KJ-300J) was used as the support in the catalyst synthesis. The carbon samples were pre-treated in an aqueous HCl solution for 24 hours to remove possible impurities. 2.0 mL aniline was first dispersed with 0.4 g acid-treated carbon black in 0.5 M HCl solution. The suspension was kept below 10 °C while the oxidant, ammonium peroxydisulfate (APS), $(NH_4)_2S_2O_8$, and transition metal precursors ($FeCl_3$ or Co $(NO_3)_2 \cdot 6H_2O$) were added. After constant mixing for 24 hours to allow the polymerized PANI to uniformly combine with the carbon black particles, the suspension containing carbon, polymer and transition metal was vacuum-dried using a rotary evaporator. The subsequent heat treatment was performed at temperatures ranging from 400 °C to 1000 °C in an inert atmosphere of nitrogen gas for one hour. The heat-treated sample was acid-leached in 0.5 M H_2SO_4 at 80 °C for 8 hours to remove unstable and inactive species from the catalyst, and then thoroughly washed in de-ionized water. In the final step, the catalyst was heat-treated again under identical conditions to the first heat treatment but for three hours instead of one.

RDE/RRDE testing

Rotating disk electrode (RDE) and rotating ring-disk electrode (RRDE) testing was performed using a CHI Electrochemical Station (Model 750b) in a conventional three-electrode cell at a rotating disk speed of 900 rpm at room temperature. The catalyst loading on RDE was controlled at 0.6 mg cm^{-2}. A graphite-rod and Ag/AgCl (3 M NaCl, 0.235 V *vs.* RHE (measured value)) were used as the counter and reference electrodes, respectively. ORR steady-state polarization curves were conducted in oxygen-saturated 0.5 M H_2SO_4 electrolyte with a potential step of 0.03 V and a period of 30 s. After 30 s, when background capacitive current had passed, the Faradaic current was measured.

In RRDE testing, the ring potential was set to 1.2 V. Before experiments, the Pt ring was activated by potential cycling in 0.5 M H_2SO_4 from 0.0 V to 1.4 V at a scan rate of 50 mV s^{-1} for 10 minutes. (RDE results collected without any source of Pt confirm high activity.) Four-electron selectivity of catalysts was evaluated based on H_2O_2 yields, calculated from the following equation:[27]

$$H_2O_2(\%) = 200 \times \frac{I_R/N}{(I_R/N) + I_D} \quad (1)$$

where I_D and I_R are the disk and ring currents, respectively, and N is the ring collection efficiency. As variations in the ring collection efficiency can occur due to differences in the type of catalyst, catalyst layer thickness, rotating speed and ionomer content, N was determined using the disk electrode loaded with PANI–Fe–C catalyst at a loading of 0.6 mg cm^{-2} and 900 rpm by reduction of ferricyanide from de-aerated 10 mM $K_3[Fe(CN)_6]$ + 0.1 M KCl electrolyte, followed by re-oxidation at the ring electrode held at 1.0 V *vs.* RHE. The disk potential was swept from 1.0 V to 0.0 V with a potential step of 0.03 V and a period of 5 s. The collection efficiency was obtained from the ring-to-disk current ratio: $N = -I_R/I_D$. Based on the geometry of the electrodes and their dimensions, the collection efficiency was expected to be 37% (as provided by the manufacturer). The determined value according to our measurements for the specific non-precious metal catalyst films used in this report was 36%.

Fuel cell testing

Non-precious metal catalysts were tested at the fuel cell cathode for ORR activity and durability under PEFC operating conditions. Cathode catalyst "inks" were prepared by ultrasonically mixing catalyst powders with Nafion® solution for four hours. The "inks" were applied to the gas diffusion layer (GDL, ELAT LT 1400W, E-TEK) by successive brushing until the cathode

catalyst loading of ~4 mg cm^{-2} was reached. The Nafion® content in the dry catalyst was maintained at *ca.* 30 wt%. A commercially available Pt-catalyzed cloth gas-diffusion layer (E-TEK, 0.25 mg cm^{-2} Pt) was used at the anode without any further processing. The cathode and anode were hot-pressed to a Nafion® 1135 membrane to fabricate the membrane–electrode assembly (MEA). The geometric active area of the MEA was 5.0 cm^2. Fuel cell testing was carried out in a single cell with single-serpentine flow channels. Hydrogen and oxygen/air, humidified at 90 °C, were supplied to the anode and cathode at flow rates of 200 and 400 mL min^{-1}, respectively. Both electrodes were maintained at the same backpressure of 2.8 bar (~3.5 bar absolute pressure at Los Alamos altitude). Fuel cell polarization plots were recorded using standard fuel cell test stations (Fuel Cell Technologies Inc.).

Physical characterization

The surface areas of the catalysts were determined by nitrogen adsorption using a Micromeritics ASAP 2010 instrument. Each sample was degassed by heating at 150 °C under vacuum prior to measuring the surface area. Because the samples have significant microporosity thus violating the assumptions of the BET model, only "apparent" BET surface areas could be obtained.[28] This was accomplished by applying the BET equation to the pressure range where the term $n(P_o - P)$ or alternatively $n(1 - P/P_o)$ was continuously increasing with P/P_o (where n is the adsorbed amount of N_2, P is the measured pressure, and P_o is the saturation pressure of nitrogen under the measurement conditions), as advised by Rouquerol *et al.*[28] when examining microporous materials. The pore size distribution (PSD) was determined from the adsorption isotherm using either nonlocal density functional theory (NLDFT) or quenched-solid density functional theory (QSDFT) with a slit pore geometry (Quantachrome® analysis software), depending on which model gave the best fit to each isotherm. All Raman spectra were obtained using a Kaiser Holospec Raman system at 514 nm excitation. Samples were prepared as powders on a glass surface, with the excitation laser focused through at 100× microscope objective for a total interrogation spot size of ~1 micron. Excitation power was held constant at ~150 μW for all samples. Scattered light was collected in backscatter configuration into an optical fiber, then dispersed through the Kaiser spectrometer and projected onto a CCD camera. Four individual 30 s spectra were summed for a total integration time of 120 s. Spectra were fit using 4 Lorentzians. Mid-infrared spectra were recorded on a Nicolet 670 FT-IR (Fourier transform infrared) spectrometer on KBr pellets. The crystallinity of various samples was determined by X-ray diffraction (XRD) using a Bruker AXS D8 Advance diffractometer with Cu Kα radiation. The patterns were obtained at a scan rate of 5° min^{-1} with a step of 0.02°. X-ray photoelectron spectroscopy (XPS) was performed at the University of New Mexico on a Kratos Axis Ultra spectrometer using a Mg Kα source operating at 150 W and monochromatic Al Kα source operating at 300 W, and charge compensation using low energy electrons. The base pressure was about 2×10^{-10} torr, and operating pressure was around 2×10^{-9} torr. The survey and high-resolution spectra were acquired at pass energies of 80 eV and 20 eV, respectively. Acquisition time for high resolution C and N 1s spectra was around 30 minutes.

The sample morphology was characterized by scanning electron microscopy (SEM) on a Hitachi S-5400 instrument. High-resolution transmission electron microscopy (HR-TEM) images were acquired using a Hitachi HF3300 TEM operated at 300 kV at Oak Ridge National Laboratory. The instrument was equipped with a secondary electron (SE) detector for the acquisition of SEM images from the same areas studied by TEM. Thermogravimetric analysis was performed using a TA Q50 instrument under a flowing dry air atmosphere. The temperature was ramped at 5 °C min^{-1} to 1000 °C and held until mass change was less than 0.05% min^{-1}, then ramped down to 25 °C at 30 °C min^{-1} during which time <0.5% mass change was observed. The residual powder was determined to be Fe_2O_3 by XRD. The mass of Fe_2O_3 was used to calculate the Fe content of the sample. Inductively coupled plasma-optical emission spectroscopy (ICP-OES) was also used to determine the catalysts' iron and cobalt content. For ICP-OES analysis, the carbon component was first removed by dry-ashing the catalysts in air at 700 °C. The ash residue was then digested in a heated mixture of trace-metal-grade concentrated hydrochloric and nitric acids (Fisher) and the resultant solution diluted with water. The iron and cobalt concentrations in the product solutions were measured using a Perkin Elmer Optima 3300 DV ICP-OES by comparison with standard solutions prepared from commercial spectroscopic solution standards (Ultra Scientific, Kingstown, RI) and were used to calculate the mass fraction of iron and cobalt in the powder sample. Fe and Co K edge X-ray absorption fine structure (XAFS) measurements were performed at the Stanford Synchrotron Radiation Lightsource on beam lines $11\bar{2}$ and $10\bar{2}$, using conventional fluorescence mode procedures. Data were analyzed and interpreted using standard procedures, with emphasis on using similar processing parameters. Metrical parameters were obtained from $\chi(k)$ by nonlinear least squares curve-fitting using amplitudes and phases calculated by FeFF, an automated program for *ab initio* multiple scattering calculations.

Results and discussion

Effect of stages in catalyst synthesis

In the catalyst synthesis, the different stages including the first heat treatment (HT1), the acid leach (AL), and the second heat treatment (HT2) play important roles in achieving good performance of PANI-derived catalysts. Results at the optimized temperature of 900 °C are discussed. The RDE and fuel cell ORR activities of PANI–Fe–C samples at different stages of the synthesis are shown in Fig. 1. Before the heat treatment (BHT), the activity of the PANI–Fe–C–BHT sample is extremely low with no significant ORR current generated until 0.3 V; the carbon support material itself is more active (Fig. 1). This suggests that few metal–nitrogen centers or other sites capable of ORR have been created by the chemical synthesis steps alone, in contrast to metal macrocycles,[29,30] metal porphyrins,[31] or even our previous work with non-heat-treated Co–PPy–C catalysts.[12] The first heat treatment creates active sites as evidenced by the marked increase in the ORR activity, with an onset potential of 0.93 V and a half-wave potential ($E_{1/2}$) of 0.67 V. The

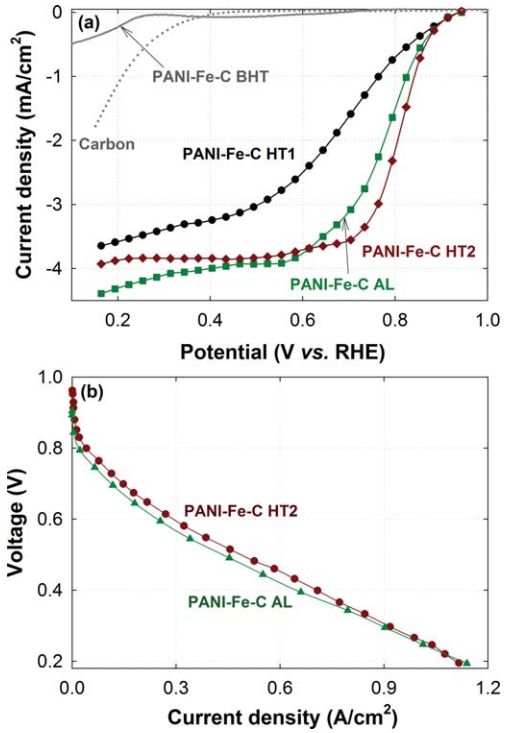

Fig. 1 (a) RDE activity and (b) fuel cell performance of PANI–Fe–C catalyst (treated at 900 °C) after the first heat-treatment (HT1), after acid leach (AL) and after the second heat-treatment (HT2).

acid-leaching step results in much higher ORR activity due to the removal of unstable phases (see Table 1 for Fe content changes) from the porous catalyst surface which presumably exposes more active sites, as shown by the shift in the $E_{1/2}$ by nearly 100 mV. However, the onset potential for ORR does not shift suggesting that the nature of the active site has not changed. Applying a second heat treatment after the acid-leaching step further improves the ORR activity as measured by both RDE (Fig. 1a) and fuel cell testing (Fig. 1b). (Fuel cell testing data for the HT1 sample are not included in Fig. 1b because of the poor fuel cell performance resulting from serious membrane contamination with Fe cations.) A positive shift of ~30 mV in $E_{1/2}$ occurs, despite some decrease in the mass-transport limited current observed at lower potentials. Yet again, the onset ORR potential does not change. This implies that neither the acid leaching nor the second heat treatment change the type of active sites present. The fuel cell performance is also enhanced by the second heat treatment as shown in Fig. 1b. In this case, the effect of HT2 on the wetting properties (hydrophilicity) of the catalyst may also be important.[32] The pattern observed for changes in the catalyst activity with processing steps (HT1, AL, HT2) has been validated for heat-treatment temperatures from 800–1000 °C.

Fig. 2 demonstrates the change in apparent BET surface area (see Experimental for details) for PANI-Fe-C catalysts at various synthesis stages. Because recent studies of NPMCs have shown a correlation between in-situ-generated microporous surface area and activity,[8,10,33,34] we also determined the microporous surface area values for these samples (Fig. 2). The apparent BET surface area and microporous surface area of the unmodified Ketjenblack (KJ-300J) supporting material are initially 860 $m^2\ g^{-1}$ and 650 $m^2\ g^{-1}$, respectively, but the *in situ* polymerization of PANI causes the surface area value to drop precipitously to 15 $m^2\ g^{-1}$. It is likely that the newly-formed polymer blocks the pores in the carbon support from being accessed by nitrogen during the gas adsorption measurement. After being subjected to a heat-treatment at 900 °C, the apparent BET surface area and microporous surface area of the catalyst notably increase to 200 $m^2\ g^{-1}$ and 230 $m^2\ g^{-1}$, respectively, either due to a partial re-opening of the carbon support pores and/or the formation of new carbon structures. The subsequent acid leaching treatment leads to another significant increase of the apparent BET and microporous surface area values to 390 $m^2\ g^{-1}$ and 300 $m^2\ g^{-1}$, respectively, which corresponds well to the observed ORR activity increase. Surface area values (apparent BET and microporous) after heat treatment and acid leaching remain much lower than

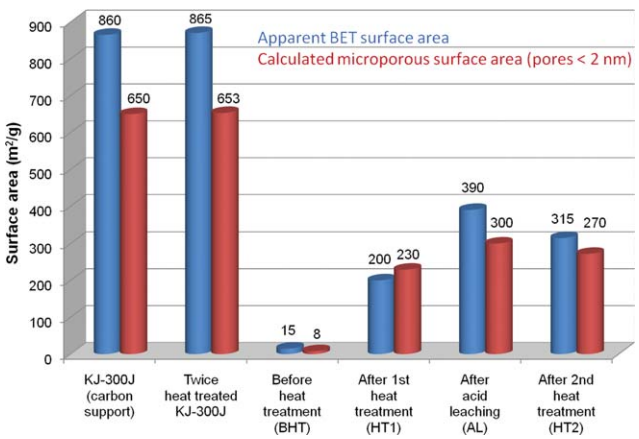

Fig. 2 Apparent BET surface areas of PANI–Fe–C catalysts as a function of synthesis stages using a heat treatment temperature of 900 °C. The BET surface areas are labeled "apparent" because the BET equation cannot give accurate estimates of surface area for microporous samples.[28] See the experimental section for details concerning the surface area estimates.

Table 1 Fe content as determined by TGA and/or ICP. The error range for the TGA and ICP measurements is around ±1% and ±0.5%, respectively. The standard deviation for the samples is ~25% of the measured value after removing outliers

	Measured Fe content (wt%)			
Expected initial Fe content (wt%) (based on calculation)	Before 1st heat treatment	After 1st heat treatment	After acid leaching	After 2nd heat treatment (as-synthesized catalyst)
3.3	4.2 (TGA and ICP)			10 (TGA)
10	12 (TGA and ICP)	38 (ICP)	31 (ICP)	12 (TGA and ICP)
20	20 (TGA)			2 (TGA and ICP)

the original carbon support, similarly to previous reports on porphyrin-based NPMCs[35,36] or bipyridine-based NPMCs[37] which attributed the surface area loss to pore blocking by decomposition products.

The second heat treatment in N_2 at 900 °C, however, results in a decrease in the apparent BET and microporous surface area values to 315 $m^2\ g^{-1}$ and 270 $m^2\ g^{-1}$, respectively, which seems contrary to the improved ORR activity that is obtained. (The reduction in surface area by HT2 may explain the slightly lower limiting current observed for the HT2 catalyst, as shown in Fig. 1.) Since the ORR onset potential does not shift, the formation of a different active site with higher activity is an unlikely explanation. It is more reasonable to assume that the active site density has increased because of the second heat treatment. This can be rationalized by considering the metal loadings observed at each stage of the synthesis as shown in Table 1. After the first pyrolysis, Fe accounts for 38 wt% of the catalyst. With such a high metal content, much of the available surface is blocked by inactive Fe forms. After removing the excess metal with acid leaching (now 3 wt% Fe), the apparent BET surface area nearly doubles (Fig. 2) and the activity greatly increases. On the other hand, the acid leaching should result in a partly oxidized catalyst surface, which could disrupt ORR active sites. The second heat treatment in N_2 can be envisioned to "repair" the partially oxidized surface at the expense of some surface area.

Recently, Koslowski *et al.*[38] also demonstrated that the catalytic activity of an already pyrolyzed material could be enhanced by a secondary heat-treatment in N_2. In contrast to our result, the surface area increased by about 40% when N_2 was used by Koslowski *et al.*[38] during the second heat treatment, and this increase correlated well to the increased activity of the treated sample without the need to assume a large increase in active site density. Because the Koslowski *et al.*[38] study used unsupported catalysts (no pores in the starting material that can close and open during synthesis), the relationship between surface area and activity was perhaps more direct. Also, the heat treatment conditions used (450 °C for 15 min, then 750 °C for 45 min, respectively) were milder and less likely to cause surface area loss. At this time, the effect of a second heat treatment under N_2 gas on NPMCs cannot be stated in a generic way. Our ongoing work with support-less catalysts will further clarify the relationship between catalyst surface area and activity.[39]

Catalysts with greatly enhanced activity after the application of a second heat treatment were also prepared by Koslowski *et al.*[38] The use of reactive gases, CO_2 or especially NH_3, during the second heat treatment was required to generate such significant increases of activity,[38] as previously applied by another group.[40] We consider the introduction of reactant gases to constitute not only a second heat treatment but also the initiation of new set of chemical reactions; therefore, catalysts generated by such means are not directly comparable to the catalysts discussed here.

To gain insight into carbon structural changes, Raman spectra were used to examine PANI–Fe–C catalysts after single and double heat-treatments at 900 °C, as compared to the Ketjenblack carbon support (Fig. 3). These spectra are dominated by characteristic carbon resonances around 1600 cm^{-1} (G band) and 1350 cm^{-1} (D band), which correspond to the planar motion of

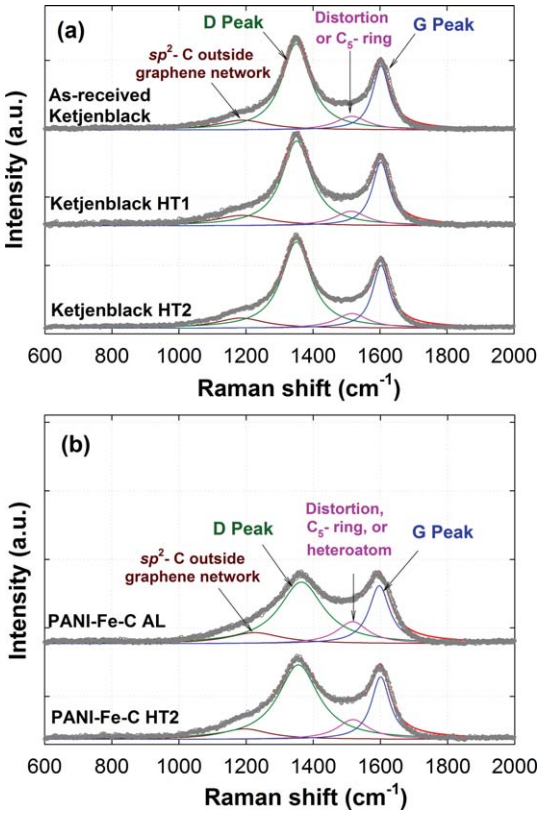

Fig. 3 Raman spectra of (a) Ketjenblack support and (b) PANI–Fe–C catalysts subjected to single and double heat-treatments at 900 °C. The singly heat treated PANI–Fe–C sample was acid leached.

sp^2-hybridized carbon atoms in an ideal graphene layer and from carbon atoms close to the edge of a graphene sheet, respectively.[41] Consequently, the ratio of these peaks gives an indication of the overall order associated with the carbon structures. Additionally, two broad signals at *ca.* 1200 and 1510 cm^{-1} are also convolved in the overall Raman spectrum. They are correspondingly associated with carbon atoms outside of a perfectly planar graphene network (such as aliphatic or amorphous structures) and integrated five-member rings or heteroatoms in graphene-sheet structures.[41,42] Each spectrum was fit to a series of four Lorentzian peaks, centered around 1200, 1350, 1510, and 1600 cm^{-1}. While the spectra for Ketjenblack that underwent the first and second heat-treatment steps show nearly identical Raman spectra, pronounced differences are observed when the PANI–Fe has been added. The intensity of the Raman bands at 1200 and 1510 cm^{-1} is significantly increased for the singly treated PANI–Fe–C catalyst (HT1) when compared to the as-received carbon; however, the relative ratio of the D band to G band is decreased. The increase in the 1200 cm^{-1} peak suggests that the carbon matrix contains a higher ratio of hydrocarbons or amorphous carbon (as expected given that a polymer was used), yet the decrease in the D-band/G-band ratio suggests that a higher proportion of carbon species with hexagonal symmetry, *i.e.*, in the interior of graphene sheets, is also present. The full-width-half-maximum (FWHM) of the D-band is also much larger, which also indicates higher disorder.[33] The Raman band at 1510 cm^{-1} indicates that the graphene layers contain distorted structures such as integrated heteroatoms within the

graphene-type lattice.[42] This is consistent with the results of the XPS analysis discussed later that confirm the presence of nitrogen heteroatoms.

The simultaneous occurrence of features in the Raman spectra that indicate "order" and "disorder" may seem counterintuitive, but several models can account for this pattern. Carbon support materials like Ketjenblack are generally depicted as spheres composed of small graphitic crystallites embedded in an amorphous carbon matrix. Just as an example, if PANI also decomposes to graphitic crystallites enclosed in an amorphous matrix, but with a larger in-plane crystallite length and with higher hydrogen content and degree of disorder in the amorphous phase, then the features of the data discussed above could occur simultaneously. Other structural models could certainly be considered, and the Raman data will be compared to high resolution XRD data and elemental analysis in the future to refine our understanding.[26,43]

After the second heat treatment, two notable changes to the Raman spectra occur: (1) an increased D-band/G-band ratio, indicating higher disorder overall, and (2) decreased FWHM of the G band (*i.e.*, narrower peak), indicating higher order within the graphitic phase.[44] The FWHM of the D band remains the same within the expected error of the fitting procedure (HT1: 157 cm^{-1} *vs.* HT2: 159 cm^{-1}). The pattern of increased activity that follows an increase in the D-band/G-band ratio (*e.g.*, more activity with more disorder) is opposite to that found by Herrmann *et al.* for sulfur-free and sulfur-added versions of their catalyst.[42] Since it is difficult to make a strong assertion of the impact of carbon structure on the catalyst activity based on the Raman data alone, a comparison of the Raman data to XRD information will be necessary to complete the structural analysis.[43]

Unlike the samples prepared by Koslowski *et al.*,[38] the PANI–Fe–C catalyst contains a carbon support, so it is instructive to compare our results to the work recently reported by the Institut National de la Recherche Scientifique (INRS). Their catalysts were prepared using a reactive gas during the second heat treatment, which is a very different synthetic path, as stated before. The synthesis began with the selection of a highly microporous carbon support.[8] The micropores were filled with phenanthroline/Fe acetate using planetary ball-milling; the material was then heat treated in Ar to create disordered carbon from the phenanthroline/Fe acetate. After some intermediate steps, the resulting precursor was heat treated in NH_3, during which time the NH_3 destroys the Fe-containing disordered carbon and leaves behind what are assumed to be Fe–N_x active sites. In this synthesis, the microporosity of the carbon support dictates the final catalyst activity that can be achieved. In the previous work by the INRS group,[33] a variety of carbon supports were used with different native disordered carbon contents. After adding Fe-containing compounds, these precursors were reacted with NH_3 gas during a heat treatment. The activity was found to correlate well with the native disordered carbon content of the carbon supports. Thus, the properties of the carbon support used—this time the disordered carbon content—again strongly controlled the activity of the catalyst that could be achieved.

In contrast, in our synthetic path the properties of the carbon support do not necessarily affect the activity. We can prepare PANI-derived catalysts of similar activity from supports with vastly different surface areas, microporosities, and initial disordered carbon content.[45] In fact, we have prepared PANI-derived catalysts with similar activity to those discussed herein using low-surface-area TiO_2 supports.[46] We interpret this to mean that the carbon phases derived from the polymer itself are capable of hosting a significant number of active sites without the need for the carbon support to act as a microporous template or to provide disordered carbon. The carbon support chosen, however, has a much larger impact on the durability, which is a subject of our ongoing study.[45]

Effect of heating temperature

The ORR activity and selectivity of the PANI-Fe-C HT2 catalysts have been found to increase with increasing heat treatment temperature from 400 °C to 900 °C and to decrease with increasing temperature from 900 °C to 1000 °C.[15] To better understand how heat treatment temperature affects the ORR activity and selectivity of these catalysts, we performed extensive physical characterization. In Fig. 4, the correlations between RDE-determined ORR activity, RRDE-determined selectivity, and surface area (apparent BET and microporous) are shown. The apparent BET surface area increases from ~40 $m^2\ g^{-1}$ for the catalyst heat-treated at 400 °C to ~300 $m^2\ g^{-1}$ for the catalyst

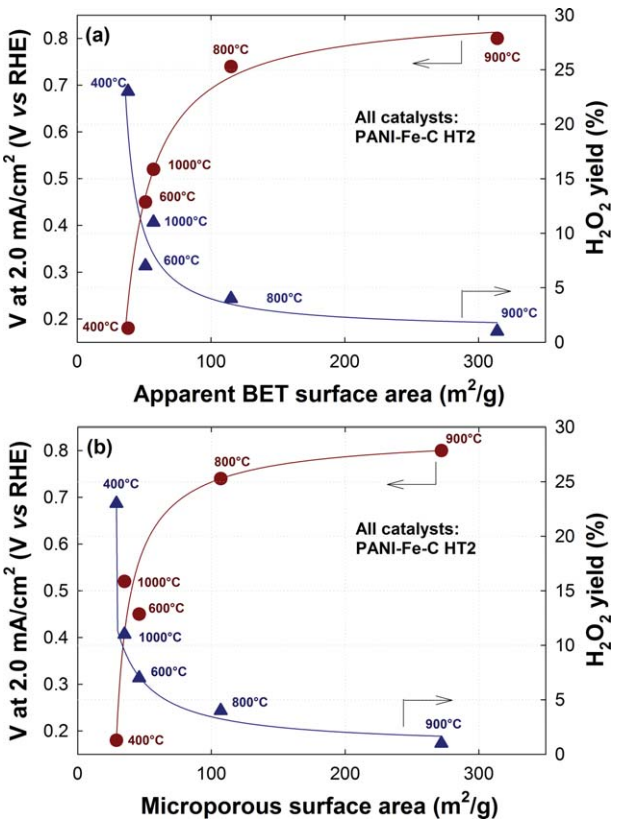

Fig. 4 (a) The correlation between catalyst activity and H_2O generation (from RRDE results) and apparent BET surface areas of PANI-Fe-C HT1 catalysts synthesized from heat-treatment temperatures ranging from 400 °C to 1000 °C, and (b) the correlation between catalyst performance and estimated microporous surface areas (pores < 2 nm diameter) of the same PANI-Fe-C catalysts. See the experimental section for details concerning the surface area estimates.

treated at 900 °C, before dropping to ~60 m^2 g^{-1} for the material treated at 1000 °C. The ORR activity and selectivity were both found to correlate well with the surface area values.

This dependence of catalyst activity on heat treatment-temperature is in agreement with an earlier work of Easton *et al.*,[47] who have investigated sputtered Fe–C–N and Co–C–N films. The authors reported that a maximum activity was achieved at 800 °C, with lower activity observed at higher annealing temperatures. Unless otherwise stated, 900 °C was selected in this work as the heat-treatment temperature for all remaining catalysts.

FT-IR spectra of the PANI-Fe-C sample before pyrolysis are in good agreement with typical polyaniline FT-IR spectra.[48,49] The peaks at 1590 and 1499 cm^{-1} can be attributed to the C–C stretching of the quinone-type (Q) and benzene-type (B) rings, respectively. The peak at 1536 cm^{-1} can be assigned to the stretching vibration of N–B–N ring. The characteristic absorption band around 1296 cm^{-1} is related to the C–N stretching of the secondary amine in the polymer main chain that exists in the conducting emeraldine-salt form. Absorption bands at 1100 cm^{-1} and 849 cm^{-1} are likely originating from the plane-bending vibrations of C–H in the structure of B–NH–Q and/or B–NH–B, and the out-of-plane bending vibration of C–H of benzene rings (B) during the protonation of HCl-doped PANI, respectively. During the heat treatment, the benzene-type and quinone-type structures on the main PANI chain decompose as evidenced by the disappearance of the relevant bands starting with the 600 °C sample (Fig. 5a). This corresponds well to the significant positive shift of ORR onset potential and sharp drop in H_2O_2 yield shown by the RRDE data.[15]

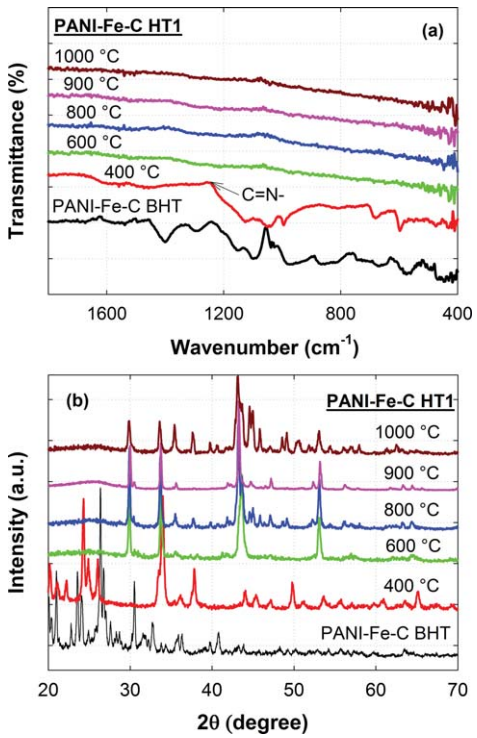

Fig. 5 Effect of heat-treatment temperature on (a) FT-IR spectra and (b) XRD patterns of PANI–Fe–C HT1 catalysts (after the first heat-treatment).

XRD was used to analyze samples after the first heat treatment (Fig. 5b). Before heat treatment, the PANI-Fe-C sample containing 10 wt% of Fe shows well-developed crystalline structures, assignable mainly to the excess of the oxidant $(NH_4)_2S_2O_8$ (2θ = 17.6°, 18.2°, 22.2°, 26.6° and 30.4°) and a small amount of iron salts (2θ = 31.2°, 36.4°, and 45.1°). The crystalline peaks for excess oxidant and PANI disappear at 600 °C, in agreement with the IR results. At the same time, large quantities of FeS (2θ = 17.1°, 18.7°, 29.9°, 31.9°, 33.7°, 35.7°, 43.3°, 47.2°, 54.0°, 63.5°, and 70.8°) appear when the heat treatment temperature reaches 600 °C; FeS becomes dominant at 900 °C. The sulfur source in the PANI-catalyst system derives from $(NH_4)_2S_2O_8$ used to polymerize aniline. Iron sulfides have been shown previously to have limited ORR activity and suffer from poor stability in acid media.[50–52] The ORR activity of iron sulfides, in terms of onset and half-wave potentials, is not comparable to that of the catalysts developed in this work. As discussed above, most of the iron sulfide is removed in the acid-leaching step, and the acid-leaching enhances rather than decreases the ORR activity.

In a recent report,[42] the addition of sulfur was shown to improve the ORR activity of a NPMC. The increased activity was attributed in part to the formation of more leachable iron sulfides as opposed to iron oxides that resulted in a higher catalyst surface area. The effect of sulfur on the carbon crystallite structure (as observed by Raman) and perhaps also sulfur heteroatom incorporation into the catalyst were suggested as additional reasons for the enhancement.[42] The PANI–Fe–C catalyst presented here may also benefit from the ease with which the iron sulfides formed during the synthesis can be leached. However, comparison to a sulfur-free version of the catalyst cannot be readily made because sulfur is introduced with the oxidant that is used to polymerize aniline; other oxidants do not create identical polymer structures. We have already begun developing sulfur-free PANI–Fe–C catalysts with high activity, the work which is ongoing.[39] As for electronic and/or chemical effects of sulfur in PANI–Fe–C, XPS analysis indicates that the sulfur predominately exists in the form of S–Fe. No S–C or S–N peaks can be detected. Possible effects of sulfur on the carbon crystallite structure cannot yet be assessed. In future work, a continuation of our recent report,[39] we will intentionally add small amounts of sulfur to an otherwise sulfur-free synthesis to better evaluate the effect of sulfur on PANI–Fe–C catalysts.

During the heat treatment at 1000 °C, XRD reveals that iron oxides (Fe_2O_3, Fe_3O_4) are formed, corresponding to the observed decrease in the ORR activity in RDE testing. The appearance of additional crystalline forms of iron implies a loss of highly dispersed active centers.

Elemental quantification of the near-surface layers of samples treated at different temperatures was performed using XPS, as shown in Fig. 6. The near-surface Fe and C contents increased with heat-treatment temperature, primarily due to the significant and expected loss of oxygen[53] and nitrogen species. Unlike the elemental contents detected by XPS, the catalyst ORR activity does not change monotonically with temperature, indicating no straightforward relationship between activity and the elemental content. The activity is not dependent on the total amount of incorporated nitrogen as elsewhere claimed.[7] Even the lowest observed nitrogen content in this study (3.5 at%) is greater than or equal to that of many other active NPMCs,[8,10,54] suggesting

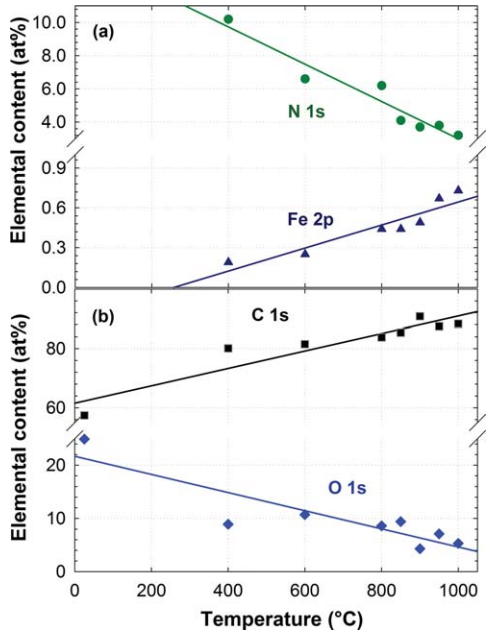

Fig. 6 Elemental quantification analysis of PANI–Fe–C catalysts using XPS: (a) Fe 2p and N 1s; (b) C 1s and O 1s. Samples are catalysts at the final stage, after the second heat treatment.

that the nitrogen content is sufficient and should not limit the activity in any of these catalysts.

Using XPS, the nitrogen speciation was analyzed for each sample treated at different temperatures as shown in Fig. 7. The content and relative ratios of different types of nitrogen, *i.e.* pyridinic (398.9 eV), quaternary (401.1 eV) and graphitic (402.9 eV), change with the heat-treatment temperature.[55] The peak at a binding energy of 398.9 eV may also include a contribution from nitrogen bound to the metal. The shift between N–Me (~399.2 eV) and N in pyridinic environment (398.2–399 eV) is quite small, making it difficult to differentiate between them quantitatively. We chose to use one peak which we will refer to as pyridinic nitrogen. It can be seen in Fig. 7 when comparing the size of pyridinic and quaternary peaks that the quaternary-to-pyridinic-nitrogen ratio rises with the heat-treatment temperature. A similar trend was also found for the PANI–Fe–TiO_2 catalyst system.[46] Based on this observation alone, one could consider quaternary nitrogen as a candidate for participating in active sites. However, because the total nitrogen content decreased with heating temperatures from 600 °C to 900 °C (Fig. 6), the *absolute* content of quaternary nitrogen does not actually increase until the temperature reaches 950 °C (higher activity is observed at lower temperatures than 950 °C). Thus, there is no readily understandable correlation between quaternary nitrogen content and the active-site density. It should be remembered, however, that the activity *vs.* elemental-content discussion in this section cannot be viewed as surface-specific in the absence of a true probe of active sites for non-precious metal catalysts.

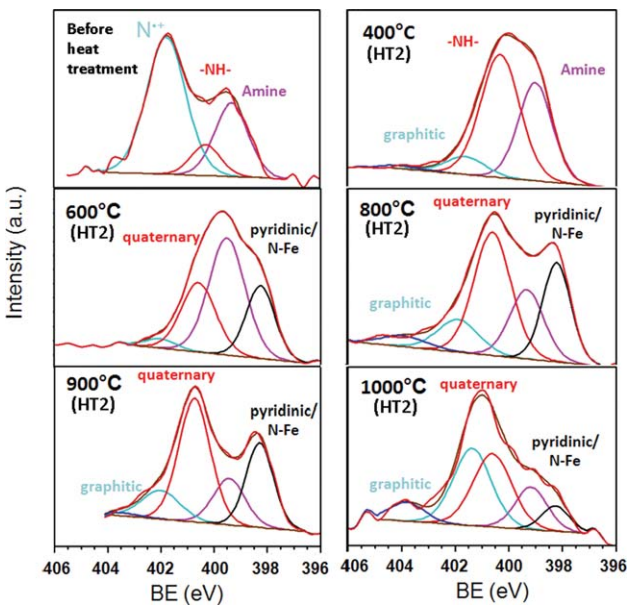

Fig. 7 N 1s spectra of PANI–Fe–C catalyst as a function of heat-treatment temperature up to 1000 °C. Samples are catalysts at the final stage, after the second heat treatment.

The catalyst morphology as a function of the heat-treatment temperature was studied using SEM and TEM (Fig. 8). The characteristic appearance of PANI nanofibers[56,57] gradually disappears as the heat-treatment temperature increases to 400 °C, and spherical particle formation begins at 600 °C. The SEM images suggest that carbon fibers with high surface area form at 900 °C. A higher degree of graphitization is also indicated by TEM images (inset), including the graphitic shells that cover the metal particles. At 1000 °C, the morphology becomes non-uniform with the formation of larger agglomerated particles compared with the original carbon black, corresponding to the significant reduction in surface area that was described earlier in the section.

Effect of the metal loading

The addition of a metal precursor is necessary for the creation of highly active ORR catalysts, and the optimal amount must be determined for each catalyst type. The Fe content in the initial reaction mixture was varied from 0.5 wt% to 20 wt% while following the synthesis procedure described in the Experimental section. Typical ORR activity curves of these catalysts are shown in Fig. 9. The ORR activity increases as the iron content increases from 0.5 wt% to 3 wt%, but the addition of more iron results in no statistically significant changes to the catalyst activity. Once the iron content is sufficient, a factor other than the iron supply limits the formation of active sites.

Compared to some previous reports,[8,58] the amount of Fe required to generate the most active catalysts is relatively high at 3 wt%. For catalysts generated by reacting ammonia gas with carbon loaded with inorganic precursors, only 0.2 wt% Fe is required for maximum activity.[59,60] In the previously-studied NH_3-generated catalysts, Fe is envisioned to populate active sites that are associated with the micropores which have been formed by reaction of the disordered carbon phase with ammonia gas. For catalysts in the present study, no ammonia gas was used and the details of the active-site formation should therefore differ. In particular, catalyst activity seems to be more strongly associated with the carbon derived from the polymer than with any features

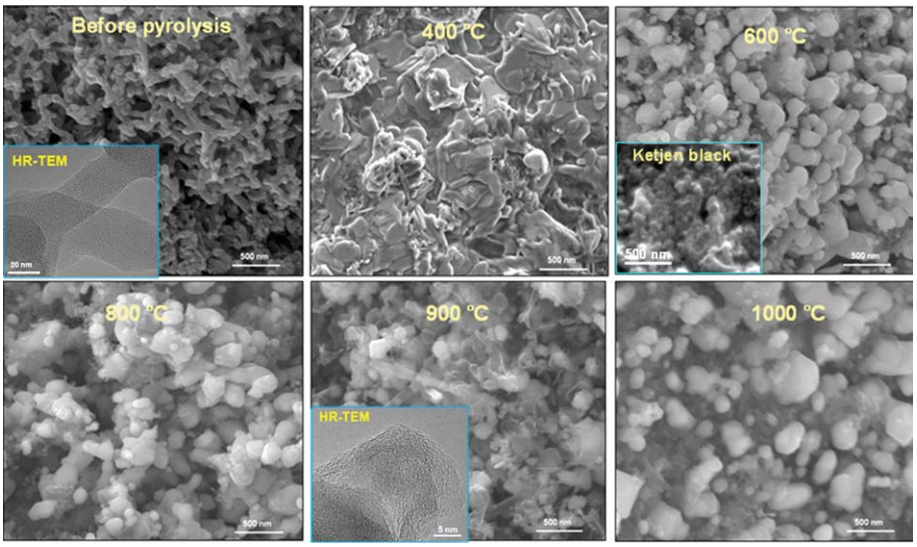

Fig. 8 SEM images of PANI–Fe–C catalyst as a function of heat-treatment temperature (scale bar for all the SEM images is 500 nm; for the HR-TEM inset in the "before pyrolysis" image is 20 nm; in the "900 °C" image is 5 nm). Samples are catalysts at the final stage, after the second heat treatment.

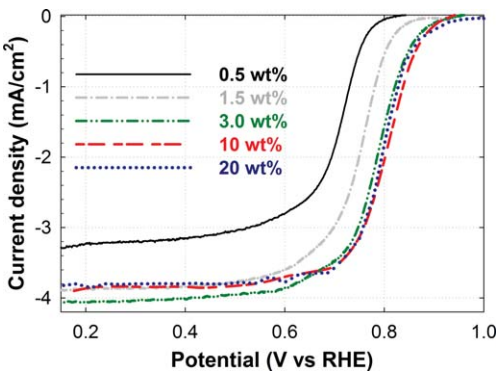

Fig. 9 Effect of nominal iron content (added in synthesis before the heat treatment) on ORR activity. The standard deviation of $E_{1/2}$ between catalyst batches is ±10 mV around average values of 0.80 V (five batches used), 0.80 V (four batches used), and 0.80 V (three batches used), respectively, making the 3 wt%, 10 wt%, and 20 wt% catalysts statistically equivalent. Three outliers were excluded from the calculation: one batch of 10 wt% catalyst and two batches of 3 wt% catalyst. Samples are catalysts at the final stage, after the second heat treatment.

of the original carbon-support material. As mentioned before, catalysts of similar activity can be obtained even with low surface area TiO_2 supports.[46] Thus, the role of the metal in these catalysts appears to be not only associated with populating the active sites (if true), but also with forming the new carbon structures from the decomposed polymer (see SEM and TEM images in the subsection below). This observation is consistent with the widespread use of transition-metal catalysts to generate carbon structures, such as nanotubes in other fields of research.[61] The need for a higher metal content in this study than for other previously reported catalyst types[59,60] can then be readily rationalized.

As shown in Table 1, the final bulk Fe content does not correlate to the ORR activity. Only a small amount of the Fe would be expected to participate in atomically dispersed active sites, ≤0.2 wt%,[10] so in all three cases a significant excess of Fe is present (2–10 wt%, see Table 1). The various excess forms of Fe apparently respond differently to the acid leaching and perhaps also to the second heat treatment, depending on the amount of Fe originally present. The 10 wt% version of the catalyst was found to be more reproducible in terms of activity than the 3 wt% version, and, unless noted otherwise, was used in the experiments presented in this report. The 20 wt% version of the catalyst was developed after most of the characterization experiments had been performed.

Effect of the transition metal

Besides the heat-treatment temperature, the ORR activities of PANI-derived catalysts are greatly dependent on the transition metals used in synthesis. Cobalt and iron salts were used to prepare PANI–Co–C and PANI–Fe–C catalysts, respectively, using 900 °C heat treatments and 10 wt% metal content in the synthesis. These two metals have been found in previous studies to generate the most active NPMCs *versus* other transition metals.[10,62] Previous RDE curves and fuel cell tests indicated that the ORR activity of the PANI-Co-C catalyst is clearly lower than that of PANI-Fe-C.[15] Here the effect of the transition metal on the catalyst durability was compared in fuel cell tests. As shown in Fig. 10, while the PANI-Co-C catalyst loses *ca.* 12% of its current density during a 200 h test, the PANI-Fe-C catalyst experiences no performance drop.

One interpretation of the high durability of these catalysts originates from the fact that the active ORR sites seem to reside in 3-D polymer-derived carbon material rather than in a very thin 2-D coating of material on a carbon support. Consequently, as the top layer of active sites is removed during electrochemical or fuel cell operation, new layers of active sites could be exposed. This explanation was also applied to the high durability of catalysts derived from phenolic resin that was recently reported.[63]

Since nitrogen incorporated into carbon is considered to be part of ORR active sites either with or without a bound metal

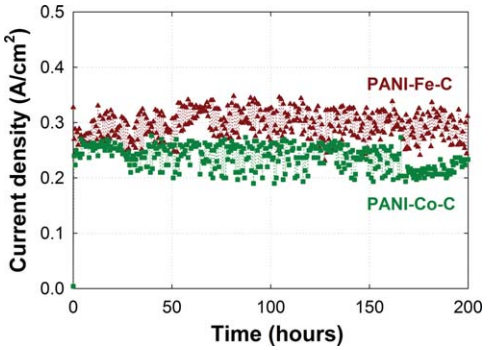

Fig. 10 Long-term fuel cell life tests at 0.40 V using H_2–air/2.8–2.8 bar. Samples are catalysts at the final stage, after the second heat treatment.

center,[8,21] the effect of transition metals on nitrogen speciation in PANI-derived catalysts was studied using XPS as shown in Fig. 11. Based on XPS elemental analysis, the N content in both Co- and Fe-based PANI–Me–C catalysts synthesized at 900 °C is very similar at ~4 to 5 at%. The use of Co instead of Fe leads to slightly higher pyridinic nitrogen content on both an absolute and relative basis. Since pyridinic nitrogen content is often correlated with ORR activity,[21] this is a notable result that the opposite pattern is observed. On the other hand, Fe increases the quaternary and pyrrolic nitrogen content slightly compared to Co on both relative and absolute scales. Similar observations were made for Fe and Co versions of a catalyst derived from ethylenediamine (EDA) (Fig. 11). Pyrrolic nitrogen has seldom been correlated with ORR activity, and quaternary nitrogen has only recently been connected either experimentally or theoretically with ORR activity.[64] (The quaternary XPS peak at *ca.* 401 eV can include contributions from graphitic nitrogen,[65] pyridinium,[66] and other nitrogen species (amines, amides),[66,67] but since this sample has been heat-treated at 900 °C, the graphitic nitrogen assignment is the most reasonable.) Recently, a metal-free catalyst was reported to show only a single peak assigned to quaternary nitrogen in the N 1s XPS spectrum,[25] but its ORR activity was much lower than that of the catalysts prepared using

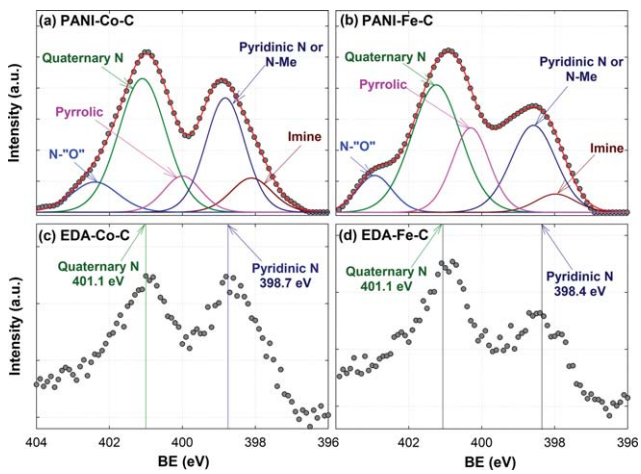

Fig. 11 N 1s spectra of XPS analysis for PANI-derived catalysts: (a) PANI-Co-C and (b) PANI-Fe-C; also for EDA-derived catalysts: (c) EDA-Co-C and (d) EDA-Fe-C.

a transition metal, such as those discussed here or reported elsewhere.[8,10] Quantum calculations on cluster models of nitrided and non-nitrided graphite sheets show that carbon radical sites formed adjacent to substitutional N in graphite are active in O_2 electro-reduction to H_2O_2.[68] Since quaternary nitrogen seems to be capable of only $2e^-$ rather than $4e^-$ reduction of oxygen according to literature, the low peroxide generation of the 900 °C PANI–Fe–C catalyst[15] makes the consideration of quaternary nitrogen as the sole active site unreasonable. Two-by-two or pseudo-four-electron[69] ORR schemes could include such a site for as long as a second site that can convert peroxide to H_2O or chemically decompose it to O_2 is also present. Alternately, quaternary nitrogen content could simply mark beneficial changes in the carbon morphology. Because we have twice seen a loose relationship between quaternary nitrogen content and catalytic activity—in the temperature study above and now when comparing Fe to Co—we believe that the abundance of quaternary nitrogen should be tracked in NPMCs, but we cannot make any strong statement about its significance.

The rather weak correlation of nitrogen content of all types (pyridinic, pyrrolic, and quaternary) and activity in these catalysts likely implies the importance of structural factors. To gain insight into the structural impact of choosing Fe *versus* Co, especially during the decomposition of PANI, the nanostructure and morphology of PANI–Fe and PANI–Co catalysts were studied using HR-TEM and SEM (Fig. 12). Graphene sheet structures are abundant in the PANI–Co–C catalyst (after the first heat-treatment, acid leaching, and the second heat-treatment), but not in the PANI–Fe–C powder. In both types of catalyst, the metal particles are coated with several layers of graphitized carbon (Fig. 12). These layers of graphitized carbon and the graphene sheets structures may or may not relate directly to ORR active sites, but a connection between these structures and activity should be considered given that the presence of "in-plane $Fe–N_4$ centers embedded in a graphene-type matrix," as determined by Mössbauer spectroscopy, has been previously correlated to the catalytic activity.[20] The significant morphological differences between the two catalysts demonstrate the strong effect of transition metal precursor selection on the carbon/nitrogen structures resulting from the heat-treatment of polymers.

XRD patterns were obtained for samples at various points in the synthesis process when Fe and Co salts were used as metal precursors and for a sample prepared without transition metal (PANI–C) (Fig. 13). Metal-free samples, including as-received carbon black, heat-treated carbon black, and PANI–C are shown in Fig. 13a. These carbon samples all show a broad (002) peak at a 2θ of *ca.* 25°, which is typical of a highly disordered carbon.[70] Heat treatment leads to an enhancement in the graphitic structure in carbon black, as shown by the sharper peak, which correlates to an improvement in the ORR activity when compared with the as-received carbon black. However, in the case of PANI–C, the formation of PANI-derived disordered carbon gives rise to a symmetric broad (002) peak, seemingly leading to an inhibition of the graphitization of the carbon black. XRD patterns for PANI–Co–C and PANI–Fe–C at different synthesis stages are compared in Fig. 13b and c, respectively. Deposition of both PANI–Fe and PANI–Co onto carbon leads to the suppression of dominant carbon peaks at 25° and 44°, and

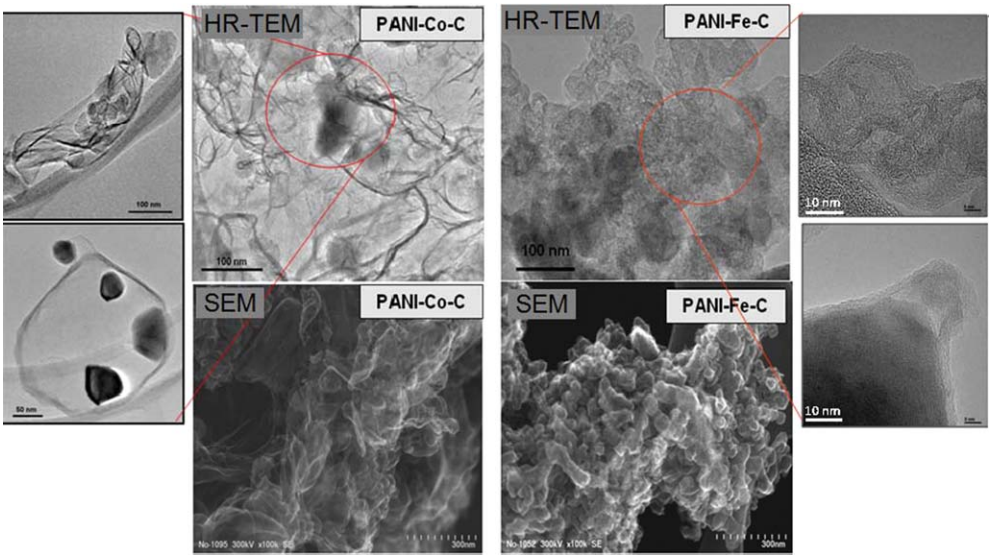

Fig. 12 HR-TEM and SEM images for PANI-Co-C and PANI-Fe-C catalysts. Samples are catalysts at the final stage, after the second heat treatment.

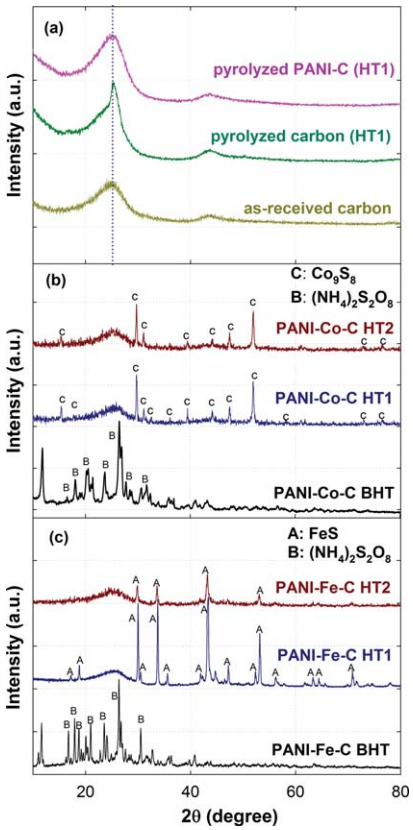

Fig. 13 XRD patterns for (a) metal-free samples, (b) PANI–Co–C, and (c) PANI–Fe–C catalysts at different stages of synthesis. All samples were prepared at 900 °C.

the appearance of well-developed crystalline structures, assignable mainly to the excess of the oxidant $(NH_4)_2S_2O_8$ ($2\theta = 17.6°$, 22.2° and 26.6°). Broad polyaniline peaks are located at 15.8°, 20.4° and 24.6°. The virtual absence of peaks attributable to cobalt and iron salts suggests that Co and Fe ions are mostly coordinated by polyaniline or adsorbed onto the carbon supports. In the case of heat-treated PANI–Co–C sample, the peaks resulting from crystalline phases can be mainly assigned to Co_9S_8 (2θ = 15.3°, 29.7°, 31.2°, 39.4°, 47.5° and 51.9°).[71] Likewise, heat treatment results in the dominant formation of FeS (2θ = 17.1°, 18.7°, 29.9°, 31.9°, 33.7°, 35.6°, 43.3°, 47.2°, 53.2° and 70.8°),[72] with some lesser contributions from metallic Fe ($2\theta = 44.8°$ and 64.2°) and Fe_3O_4 ($2\theta = 41.9°$, 56.3° and 63.1°) for the PANI–Fe–C case. After leaching these heat-treated samples in 0.5 M H_2SO_4 at 80 °C for 8 hours and performing a second heat treatment, the FeS in PANI–Fe–C greatly decreases, unlike the Co_9S_8 peaks in the PANI–Co–C catalyst. For the reduced iron content version of the sample used for the XAS experiments below (3 wt% *vs.* 10 wt%), the FeS peaks completely disappear. In contrast to the cobalt, much of the iron exists in a non-crystalline form.

Ex situ XAFS was used to analyze the coordination environment of transition metals in the PANI–Co–C and PANI–Fe–C catalysts (Fig. 14), in an attempt to identify non-crystalline species. Samples with 3 wt% Fe and Co content were prepared to decrease interference from spectator species *versus* the typical 10 wt% catalysts. The metal content of PANI–Co–C catalyst was similar to PANI–Fe–C at *ca.* 10 wt%. Overlaying the Fe and Co EXAFS (Fig. 14a, $\chi(R)$ representation) shows that the average environments of the two metals are completely different. The Fe spectrum displays only a single, low amplitude peak at short R (R = distance from Fe atom) and no long-range order, whereas the Co exhibits extended order and a nearest neighbor at a significantly longer distance. Both the PANI–Co–C and PANI–Fe–C EXAFS spectra (Fig. 14b and c) could be fit using metal, sulfur, and oxygen/nitrogen coordination shells. (The EXAFS signals from O and N in the local environment of the metal are equivalent to each other in these data, causing their contribution to be labeled O/N.) Consistent with the XRD, the Co EXAFS is well fit (Fig. 14b) by a series of neighbor shells that correspond well with those of Co_9S_8, as shown in Fig. 14d.[73] This assignment is corroborated by the direct comparison of the experimental spectrum with that calculated for this compound.

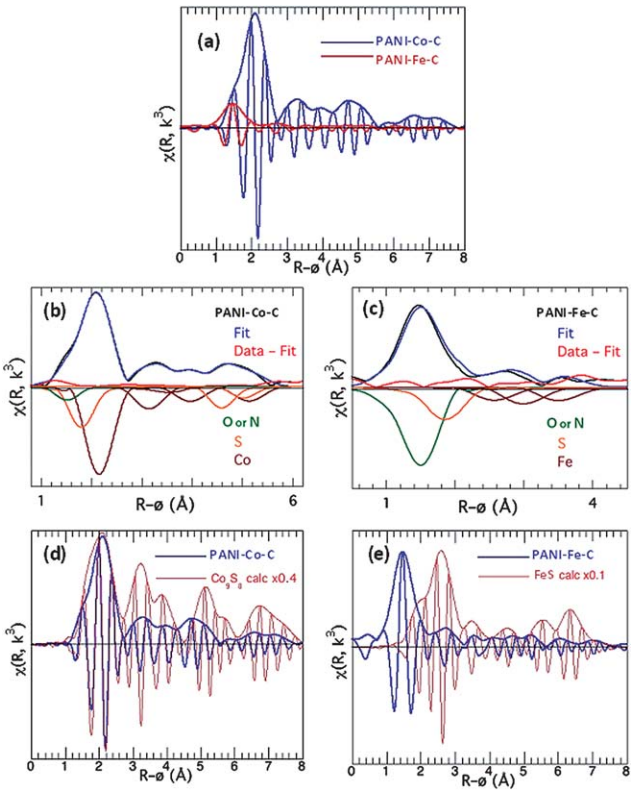

Fig. 14 The radial distribution functions (RDFs) of (a) PANI–Fe–C and PANI–Co–C, (b) PANI–Co–C and (c) PANI–Fe–C catalysts. (d and e) Comparison of the catalyst RDFs to the RDFs of metal sulfides. Samples are catalysts at the final stage, after the second heat treatment.

Although, unsurprisingly, the EXAFS of the Co in the catalyst material is lower in amplitude and thus less ordered than the pure mineral, it is nevertheless evident that the preponderance of the Co resides in the Co_9S_8 found by diffraction with only a small fraction in other forms. These other forms, however, are likely to be important because Co_9S_8 cannot account for the observed degree of ORR activity. It is therefore worth noting the relatively small O shell at 1.5 Å and the possible S shell at 1.8 Å that does not belong to Co_9S_8.

The most prominent feature in the Fe EXAFS is the near-neighbor peak at $R = 1.5$ Å that is well fit primarily by an O/N, a distance typical of the Fe–N_4 structures that occur in N-based macrocyclic ligands.[74–76] The fit also finds a sulfur shell at 1.8 Å and then the possibility of Fe shells at longer distances. However, a direct comparison of the experimental EXAFS with that calculated for FeS (Fig. 14e) as a candidate iron sulfide analogous to the formation of a cobalt sulfide *via* the same preparation method indicates that FeS does not account for a significant amount of the Fe in the material.

Fe–N_x bonds can certainly be considered, then, as a strong possibility for the dominant Fe structure in the PANI–Fe–C catalyst, whereas Co–N_x bonds are clearly not the dominant Co structure in the PANI–Co–C catalyst. Co–N_x bonds may be present at a sufficiently high number to remain as candidates for active sites, however, given that the overall intensity of the radial distribution function (RDF) is much larger for PANI–Co–C than for PANI–Fe–C (Fig. 14a). In other words, the shell attributed to Co–(O/N) coordination is non-negligible when compared on an absolute scale to the PANI–Fe–C RDF. PANI–Co–C catalysts with a lower content of spectator species must be prepared before any further conclusion can be drawn.

Conclusion

In this work, an active and durable NPMC for the ORR was developed based on the heat treatment of polyaniline, metal salt, and a carbon support through a systematic approach. The active sites are formed in a heat-treatment step, and thus the activity is greatly dependent on the selected heat-treatment temperature in the catalyst synthesis. 900 °C is the most suitable heat-treatment temperature because significant graphitization is achieved without the excessive surface area loss and active site decomposition that occur at higher temperatures. No simple correlation between activity and nitrogen content was found by XPS, because a sufficient quantity of nitrogen (and nitrogen subspecies) is present in all the catalysts. Another factor controls the performance, which is most likely the catalyst morphology. The marked changes in the carbon structure that correspond to large activity differences, the lack of a strong dependence of activity on the support chosen, and the relatively high metal loading needed to achieve an active catalyst—these observations all point to the importance of the metal-catalyzed transformation of the polymer into new carbon forms for the catalyst performance. Future work should focus on a more precise control of the metal/polymer interaction during the thermal decomposition. For example, controlling the morphology of the polymer during the synthesis or monitoring the metal particle size formed during the heat treatment can lead to different catalytic outcomes.[39]

In the PANI-derived catalyst family, the use of cobalt in the synthesis leads to much lower activity than the use of iron. The polymer is predominately transformed into graphitized structures; future study will attempt to establish the correlation between observed carbon structure and performance. According to EXAFS, Co–$(O/N)_x$ structures are clearly not the dominant form of cobalt in PANI–Co–C. These species are present at a sufficient level, however, that they remain a candidate for the active site. On the other hand, the Fe–$(O/N)_x$ coordination environment dominates the PANI–Fe–C samples, suggesting that Fe–N_x structures analogous to traditional macrocyclic ORR catalysts could exist in PANI–Fe–C. Additional, surface-specific information would be required for a concrete assignment of the active sites, which will be pursued in future work.

Acknowledgements

We are grateful to Drs Jerzy Chlistunoff, Fernando Garzon, Rangachary Mukundan, and Hoon Chung at LANL for relevant discussions. Financial support for this work has been provided by the DOE-EERE Fuel Cells Technologies Program (Technology Development Manager: Nancy Garland) and the Los Alamos National Laboratory through Laboratory-Directed Research and Development program (LDRD). Portions of this research were carried out at the Stanford Synchrotron Radiation Lightsource, a national user facility operated by Stanford University on behalf of the US Department of Energy, Office of Basic Energy Sciences. Microscopy research was supported by

Oak Ridge National Laboratory's SHaRE User Facility, which is sponsored by the Scientific User Facilities Division, Office of Basic Energy Sciences, the US Department of Energy.

References

1 H. A. Gasteiger, S. S. Kocha, B. Sompalli and F. T. Wagner, *Appl. Catal., B*, 2005, **56**, 9–35.
2 R. Jasinski, *Nature*, 1964, **201**, 1212.
3 D. Villers, X. Jacques-Bedard and J. P. Dodelet, *J. Electrochem. Soc.*, 2004, **151**, A1507–A1515.
4 S. Maldonado and K. J. Stevenson, *J. Phys. Chem. B*, 2004, **108**, 11375.
5 G. Wu, Z. W. Chen, K. Artyushkova, F. H. Garzon and P. Zelenay, *ECS Trans.*, 2008, **16**, 159–170.
6 G. Wu, C. S. Dai, D. L. Wang, D. Y. Li and N. Li, *J. Mater. Chem.*, 2010, **20**, 3059–3068.
7 V. Nallathambi, J. W. Lee, S. P. Kumaraguru, G. Wu and B. N. Popov, *J. Power Sources*, 2008, **183**, 34–42.
8 M. Lefevre, E. Proietti, F. Jaouen and J. P. Dodelet, *Science*, 2009, **324**, 71–74.
9 P. H. Matter, E. Wang and U. S. Ozkan, *J. Catal.*, 2006, **243**, 395.
10 F. Jaouen, J. Herranz, M. Lefevre, J. P. Dodelet, U. I. Kramm, I. Herrmann, P. Bogdanoff, J. Maruyama, T. Nagaoka, A. Garsuch, J. R. Dahn, T. Olson, S. Pylypenko, P. Atanassov and E. A. Ustinov, *ACS Appl. Mater. Interfaces*, 2009, **1**, 1623–1639.
11 G. Wu, K. Artyushkova, M. Ferrandon, J. Kropf, D. Myers and P. Zelenay, *ECS Trans.*, 2009, **25**, 1299–1311.
12 R. Bashyam and P. Zelenay, *Nature*, 2006, **443**, 63–66.
13 F. Jaouen, E. Proietti, M. Lefèvre, R. Chenitz, J.-P. Dodelet, G. Wu, H. T. Chung, C. M. Johnston and P. Zelenay, *Energy Environ. Sci.*, 2011, **4**, 114–130.
14 H. T. Chung, C. M. Johnston, F. H. Garzon and P. Zelenay, *ECS Trans.*, 2008, **16**, 385–391.
15 G. Wu, K. L. More, C. M. Johnston and P. Zelenay, *Science*, 2011, **332**, 443–447.
16 R. Kothandaraman, V. Nallathambi, K. Artyushkova and S. C. Barton, *Appl. Catal., B*, 2009, **92**, 209–216.
17 T. Ikeda, M. Boero, S. F. Huang, K. Terakura, M. Oshima and J. Ozaki, *J. Phys. Chem. C*, 2008, **112**, 14706–14709.
18 S. Pylypenko, S. Mukherjee, T. S. Olson and P. Atanassov, *Electrochim. Acta*, 2008, **53**, 7875–7883.
19 C. W. B. Bezerra, L. Zhang, K. Lee, H. Liu, A. e. L. B. Marques, E. P. Marques, H. Wang and J. Zhang, *Electrochim. Acta*, 2008, **53**, 4937.
20 U. I. Koslowski, I. Abs-Wurmbach, S. Fiechter and P. Bogdanoff, *J. Phys. Chem. C*, 2008, **112**, 15356–15366.
21 P. H. Matter, L. Zhang and U. S. Ozkan, *J. Catal.*, 2006, **239**, 83–96.
22 S. Maldonado, S. Morin and K. J. Stevenson, *Carbon*, 2006, **44**, 1429.
23 N. P. Subramanian, X. G. Li, V. Nallathambi, S. P. Kumaraguru, H. Colon-Mercado, G. Wu, J. W. Lee and B. N. Popov, *J. Power Sources*, 2009, **188**, 38–44.
24 T. S. Olson, S. Pylypenko, J. E. Fulghum and P. Atanassov, *J. Electrochem. Soc.*, 2010, **157**, B54–B63.
25 T. Iwazaki, R. Obinata, W. Sugimoto and Y. Takasu, *Electrochem. Commun.*, 2009, **11**, 376–378.
26 M. Ferrandon, G. Wu, K. Artyushkova, K. L. More, U. Kramm, A. J. Kropf, E. Brosha, P. Bogdanoff, C. M. Johnston, D. J. Myers and P. Zelenay, in preparation.
27 S. L. Gojkovic, S. Gupta and R. F. Savinell, *Electrochim. Acta*, 1999, **45**, 889.
28 J. Rouquerol, P. Llewellyn and F. Rouquerol, in Stud. Surf. Sci. Catal., ed. F. R.-R. J. R. P. L. Llewellyn and N. Seaton, Elsevier, 2007, pp.49–56.
29 J. Zagal, M. Paez, A. A. Tanaka, J. R. Dossantos and C. A. Linkous, *J. Electroanal. Chem.*, 1992, **339**, 13–30.
30 R. Baker, D. P. Wilkinson and J. Zhang, *Electrochim. Acta*, 2008, **53**, 6906–6919.
31 J. P. Collman, P. Denisevich, Y. Konai, M. Marrocco, C. Koval and F. C. Anson, *J. Am. Chem. Soc.*, 1980, **102**, 6027–6036.
32 G. Wu and B. Q. Xu, *J. Power Sources*, 2007, **174**, 148–158.
33 F. Charreteur, F. Jaouen, S. Ruggeri and J. P. Dodelet, *Electrochim. Acta*, 2008, **53**, 2925–2938.
34 F. Jaouen, M. Lefèvre, J.-P. Dodelet and M. Cai, *J. Phys. Chem. B*, 2006, **110**, 5553–5558.
35 G. Q. Sun, J. T. Wang, S. Gupta and R. F. Savinell, *J. Appl. Electrochem.*, 2001, **31**, 1025–1031.
36 Y. Kiros, *Int. J. Electrochem. Soc.*, 2007, **2**, 285–300.
37 R. Kothandaraman, V. Nallathambi, K. Artyushkova and S. C. Barton, *Appl. Catal. B—Environ.*, 2009, **92**, 209–216.
38 U. I. Koslowski, I. Herrmann, P. Bogdanoff, C. Barkschat, S. Fiechter, N. Iwata, H. Takahashi and H. Nishikori, *ECS Trans.*, 2008, **13**, 125–141.
39 Z. Ding, C. M. Johnston and P. Zelenay, *ECS Trans.*, 2010, **33**, 565–577.
40 J. Fournier, G. Lalande, R. Cote, D. Guay and J. P. Dodelet, *J. Electrochem. Soc.*, 1997, **144**, 218–226.
41 F. Tuinstra and J. L. Koenig, *J. Chem. Phys.*, 1970, **53**, 1126–1130.
42 I. Herrmann, U. I. Kramm, J. Radnik, S. Fiechter and P. Bogdanoff, *J. Electrochem. Soc.*, 2009, **156**, B1283–B1292.
43 A. Cuesta, P. Dhamelincourt, J. Laureyns, A. Martinez-Alonso and J. M. D. Tascon, *J. Mater. Chem.*, 1998, **8**, 2875–2879.
44 A. Sadezky, H. Muckenhuber, H. Grothe, R. Niessner and U. Pöschl, *Carbon*, 2005, **43**, 1731–1742.
45 P. Zelenay, in *2010 Merit Review and Peer Evaluation Meeting: Hydrogen, Fuel Cells & Infrastructure Technologies Program*, US Department of Energy, Energy Efficiency and Renewable Energy, Arlington, Virginia, 2010.
46 G. Wu, M. A. Nelson, N. H. Mack, S. Ma, P. Sekhar, F. H. Garzon and P. Zelenay, *Chem. Commun.*, 2010, **46**, 7489–7491.
47 E. B. Easton, R. Z. Yang, A. Bonakdarpour and J. R. Dahn, *Electrochem. Solid-State Lett.*, 2007, **10**, B6–B10.
48 S. Zhou, T. Wu and J. Q. Kan, *J. Appl. Polym. Sci.*, 2007, **106**, 652–658.
49 M. Baibarac, I. Baltog, S. Lefrant, J. Y. Mevellec and O. Chauvet, *Chem. Mater.*, 2003, **15**, 4149–4156.
50 L. Zhu, D. Susac, M. Teo, K. C. Wong, P. C. Wong, R. R. Parsons, D. Bizzotto, K. A. R. Mitchell and S. A. Campbell, *J. Catal.*, 2008, **258**, 235–242.
51 R. A. Sidik and A. B. Anderson, *J. Phys. Chem. B*, 2006, **110**, 936.
52 D. Susac, L. Zhu, M. Teo, A. Sode, K. C. Wong, P. C. Wong, R. R. Parsons, D. Bizzotto, K. A. R. Mitchell and S. A. Campbell, *J. Phys. Chem. C*, 2007, **111**, 18715–18723.
53 G. de la Puente and J. A. Menéndez, *Solid State Ionics*, 1998, **112**, 103–111.
54 Y. Nabae, S. Moriya, K. Matsubayashi, S. M. Lyth, M. Malon, L. Wu, N. M. Islam, Y. Koshigoe, S. Kuroki, M.-a. Kakimoto, S. Miyata and J.-i. Ozaki, *Carbon*, 2010, **48**, 2613–2624.
55 G. Wu, D. Y. Li, C. S. Dai, D. L. Wang and N. Li, *Langmuir*, 2008, **24**, 3566–3575.
56 G. Wu, L. Li, J.-H. Li and B.-Q. Xu, *Carbon*, 2005, **43**, 2579.
57 G. Wu, L. Li, J.-H. Li and B.-Q. Xu, *J. Power Sources*, 2006, **155**, 118.
58 F. Jaouen and J. P. Dodelet, *Electrochim. Acta*, 2007, **52**, 5975–5984.
59 M. Lefévre, J. P. Dodelet and P. Bertrand, *J. Phys. Chem. B*, 2000, **104**, 11238–11247.
60 H. Wang, R. Cote, G. Faubert, D. Guay and J. P. Dodelet, *J. Phys. Chem. B*, 1999, **103**, 2042–2049.
61 S. B. Sinnott, R. Andrews, D. Qian, A. M. Rao, Z. Mao, E. C. Dickey and F. Derbyshire, *Chem. Phys. Lett.*, 1999, **315**, 25–30.
62 Y. Feng and N. Alonso-Vante, *Phys. Status Solidi B*, 2008, **245**, 1792–1806.
63 L. Wu, Y. Nabae, S. Moriya, K. Matsubayashi, N. M. Islam, S. Kuroki, M.-a. Kakimoto, J.-i. Ozaki and S. Miyata, *Chem. Commun.*, 2010, **46**, 6377–6379.
64 E. Vayner and A. B. Anderson, *J. Phys. Chem. C*, 2007, **111**, 9330–9336.
65 K. Stanczyk, R. Dziembaj, Z. Piwowarska and S. Witkowski, *Carbon*, 1995, **33**, 1383–1392.
66 J. R. Pels, F. Kapteijn, J. A. Moulijn, Q. Zhu and K. M. Thomas, *Carbon*, 1995, **33**, 1641–1653.
67 B. Stohr, H. P. Boehm and R. Schlogl, *Carbon*, 1991, **29**, 707–720.
68 R. A. Sidik, A. B. Anderson, N. P. Subramanian, S. P. Kumaraguru and B. N. Popov, *J. Phys. Chem. B*, 2006, **110**, 1787–1793.
69 J. D. Wiggins-Camacho and K. J. Stevenson, *J. Phys. Chem. C*, 2009, **113**, 19082–19090.
70 H. Shi, J. N. Reimers and J. R. Dahn, *J. Appl. Crystallogr.*, 1993, **26**, 827–836.
71 V. Rajamani and C. T. Prewitt, *Can. Mineral.*, 1975, **13**, 75.

72 H. E. King and C. T. Prewitt, *Acta Crystallogr., Sect. B: Struct. Crystallogr. Cryst. Chem.*, 1982, **38**, 1877.
73 S. M. A. M. Bouwens, J. A. R. Van Veen, D. C. Koningsberger, V. H. J. De Beer and R. Prins, *J. Phys. Chem.*, 1991, **95**, 123–134.
74 S. Kim, T. Ohta and G. Kwag, *Bull. Korean Chem. Soc.*, 2000, **21**, 588.
75 S. H. Choi, B. R. Wood, J. A. Ryder and A. T. Bell, *Phys. Scr., T*, 2005, **115**, 688.
76 J. Yang, D.-J. Liu, N. N. Kariuki and L. X. Chen, *Chem. Commun.*, 2008, 329.